Supplementary materials for

Geometry of obstructed pathway regulates upstream navigational pattern of sperm population

Ali Karimi, Mohammad Yaghoobi, Alireza Abbaspourrad*

Department of Food Science and Technology, Cornell University, Ithaca, NY 14853, USA.

*Corresponding author: alireza@cornell.edu

Table of Contents

S1. Microfluidic design of obstructed pathways

To simulate the constructed pathways in the Fallopian tube, we designed an array of micro-barriers (N=10), mimicking a segment of the pathway, located at the middle of a wide channel with inlet and outlet ports (Figure S1.a). The main design and sperm processing procedure is inspired from a previous work(*1*). Chips with various barrier geometries were fabricated with conventional soft lithography (Figure S1.b).
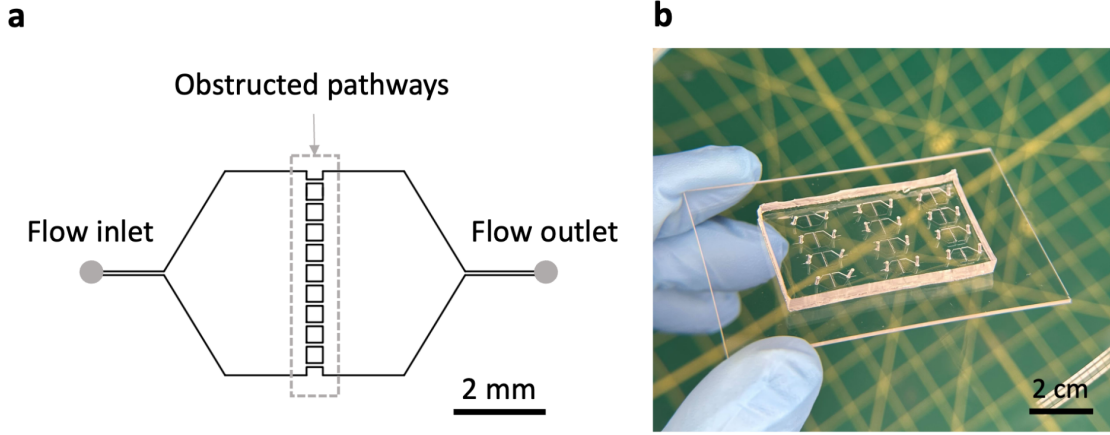

Figure S1. (a) Schematic design of microfluidic chip used to study sperm navigation in obstructed pathways. (b) Multi-chip microfluidic device containing obstructed pathways with different geometries. Scale bar indicates 2 cm.

S2. Image processing and analysis workflow

To extract pixels containing sperm and excluding the background noise, we used a multi-step image processing procedure. An example image processing workflow on a video of sperm motion in a 45°-tapered barrier with port size of 130 μm is shown in Figure S2. The movie is initially imported to ImageJ software, the brightness is adjusted, and the following z-projection filters were applied consecutively. 1) Minimum Intensity Projection (MIP) generates an output image where each pixel holds the lowest value from all images in the stack at that specific pixel location (x,y).

$$I_{min}(x, y) = (I_1(x, y), I_2(x, y), I_3(x, y), \dots, I_N(x, y))$$

This projection extracts sperm from each frame and overlays them in a single image. 2) Median projection (MP) generates an image where each pixel retains the median intensity from all images in the stack at the respective pixel location. For an even number of frames (N), the median can be calculated by the following equation.

$$I_{MP}(x, y) = \frac{I_{\frac{N}{2}} + I_{\frac{N}{2}+1}}{2}$$

This filter extracts the background stationary pixels among the frames. 3) Standard Deviation projection (STDP) produces a real image displaying the standard deviation across the slices. $\underline{I}(x, y)$ is the average intensity calculated at position (x,y).

$$I_{STD}(x, y) = \sqrt{\frac{\sum_{i=1}^{N} \left(I_i(x, y) - \underline{I}(x, y)\right)^2}{N}}$$

This filter was applied to a new stack consisting of the images resulting from MIP and MP projections.
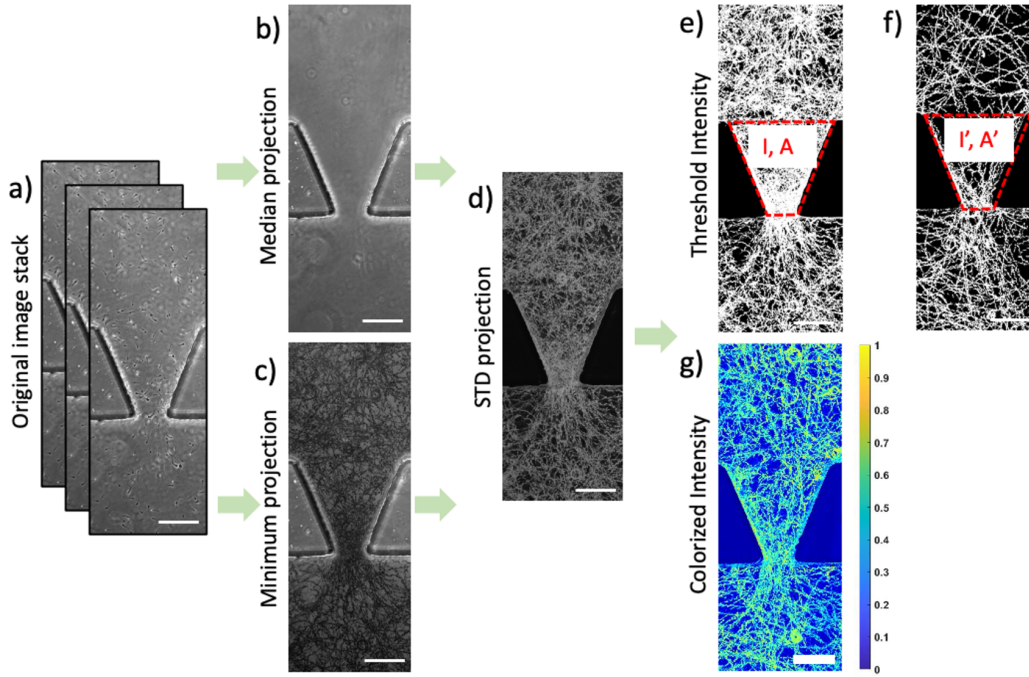

Figure S2. Image analysis workflow used for analysis of frames of video of sperm motion in a 45°- tapered barrier with port size of 130 µm under shear rate of 8 s^{-1}. (a) original video file containing 100 frames– 5 seconds of sperm motion. Median (b) and minimum (c) projections are applied separately to the image stack. The resulting two images were converted into a new stack and the standard deviation projection (d) is applied to extract pixels containing sperm presence over time. The gray-scale image was set to black/white intensity to display all sperm trajectories in white (e). The intensities and corresponding areas are measured for two cases: in presence of fluid flow (e) and in absence of fluid flow (f). The gray-scale images were also colorized for enhanced visualization (g).

For calculation of the Accumulation Index, many sperm were swimming near the wall and due to light refraction, it was impossible to use the same particle analysis approach. Hence, we developed an intensity-based calculation of sperm presence inside the barrier to facilitate the process. The gray-scale image resulting from the previous image processing procedure was set to black/white to display all pixels that contained sperm projections in white. The mean intensity (I) and area (A, in square pixels) inside the barrier were measured using ImageJ (Figure S 2.e and f). The same procedure was applied for the no-flow condition as well to obtain I' and A'.
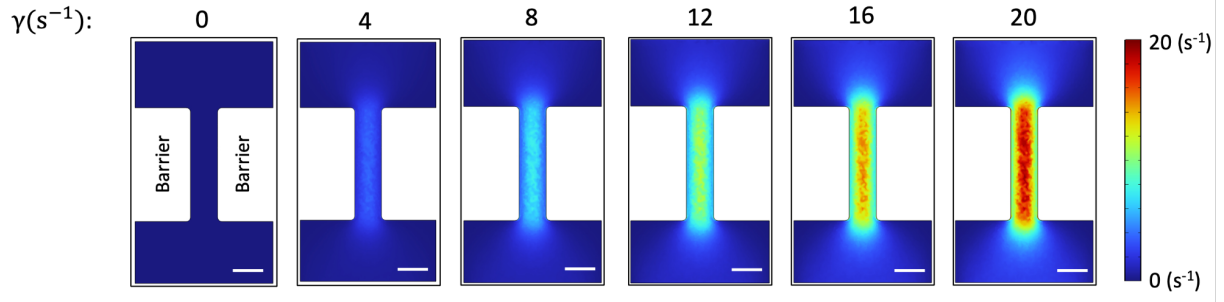
S3. dynamic of sperm navigation

Figure S3. Shear rate profiles of straight barriers under different flow conditions extracted from simulations in COMSOL software. Scale bar and color bar indicate 100 μm and local shear rate, respectively.

To study the dynamic response of sperm population to a step change in shear rate, we used the straight barrier configuration and established a sperm population in proximity of barriers by using shear rate of 8 s^{-1}. Then, the flow was stopped, and the sperm distribution was monitored on both sides of a set of three barriers (video acquisition at 1 fps for 90 seconds). Flow is connected at t = 0 s.
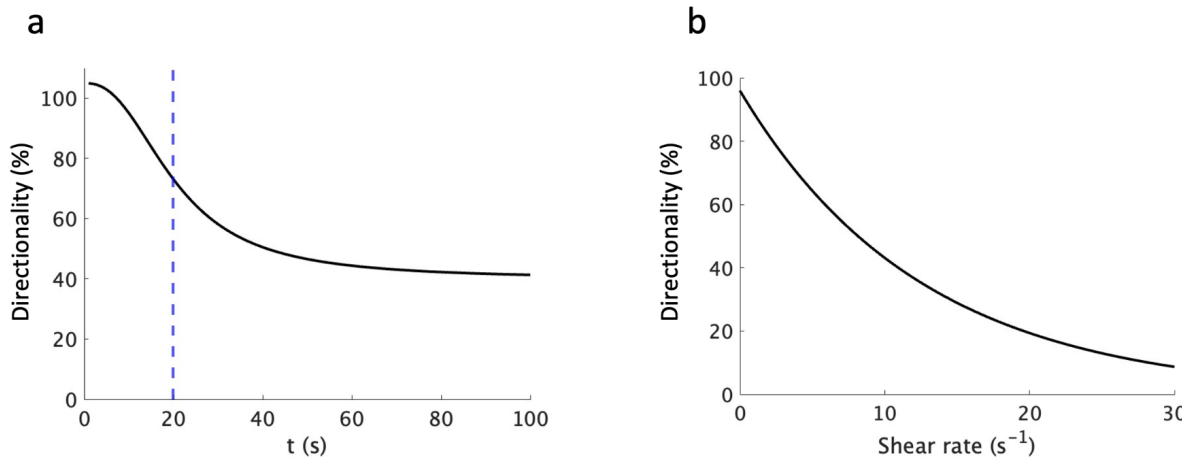
Figure S4. Analysis of the response of the sperm population distribution for a straight barrier with port size of 95 μm. Dynamic response (fitted curve) of sperm population to a step change in shear rate with magnitude of 8 s^{-1} applied at t = 0 s (a). The blue dashed line represents the time constant (τ) of the fitted curve. Dependency of directionality on shear rate fitted to an exponential decay function.

The response of the sperm navigation to fluid flow can be fitted ($R^2 = 0.89$) to four-parameter logistic equation (Figure S4)

$$directionality\% \, (t) = d + \frac{a - d}{1 + \left(\frac{t}{c}\right)^{b}}$$

where t is time, a is theoretical value for steady-state navigation (a = 40 %), b is slope factor (b = –2.4), c is time required to reach 50% of final directionality (c =20 s), and d is theoretical directionality in absence of fluid flow (d = 105 %). In this case, time constant (τ) is calculated by τ = c = 20 s. Time lag time and steady-state time is calculated by t_{lag} = τ/2 = 10 s and $t_{s.s.}$ = 2* τ = 40 s. The lag time might be hypothetically due to the lagged response of syringe pump or the intrinsic lag time of sperm to reorient in the transition zones at barrier corners.

Directionality was fitted to an exponential decay function (R^2 = 0.89) to explain its correlation with shear rate (Figure S4.b)

$$\%directionality\ (\gamma) = a \times e^{-b\gamma}$$

where a and b are directionality in the absence of fluid flow (a = 96%) and decay constant (b = – 0.1), respectively.

S4. Effect of temperature on scattering angle at corners

Sperm interaction with surfaces, especially the scattering angle when facing a sharp corner, depends on temperature. To investigate the effect of temperature on scattering angle, we used the straight barrier and established a sperm population by washing a semen sample with portal shear rate of 8 s^{-1} at 37 °C. Next temperature was set to 30 °C and the sperm locomotion under no flow condition was captured. The same experiment was conducted for higher temperatures of 37 °C and 44 °C using the same sperm population (Movie S1 compares sperm motion for two temperatures). A comparison sperm trajectories was overlayed using a 10-frame video (Figure S5).

The sperm population motility decreased in lower temperatures, while at higher temperatures, due to elevated rotational diffusion, sperm had higher surface interaction (higher intensity on surfaces and near corners). The scattering angle of sperm at corners is calculated at different temperatures (Figure S5.b). A minimum number of 20 sperm is measured for the distributions. Scattering angle was significantly larger at 37 °C compared to 30 °C (Two-sample Kolmogorov-Smirnov test, p < 0.00001). However, the scattering angle did not significantly change by increasing temperature from 37 °C to 44 °C (p > 0.05).

We also compared the level of motility of the sperm population at different temperatures by measuring the average intensity of black/white overlayed image (see section S1 for more information) extracted from a 5 second video. Figure S5c compares the average motility representative of sperm populations at various temperatures. Motility increased when temperature was elevated. This is consistent with previous studies reporting that temperature elevation enhanced sperm linear velocity and lowered the frequency of turning events in human sperm trajectory (*2*). The distinct behavior of sperm at different temperatures is reported to be a potential method to perform sperm sexing, as the X-chromosome-bearing human sperm are reported to be enriched at higher temperatures(*3*). Hence, we suggest that the combination of the surface interaction, rheotaxis, and temperature dependent motion of sperm in microenvironments can be a potential method for sperm sexing.
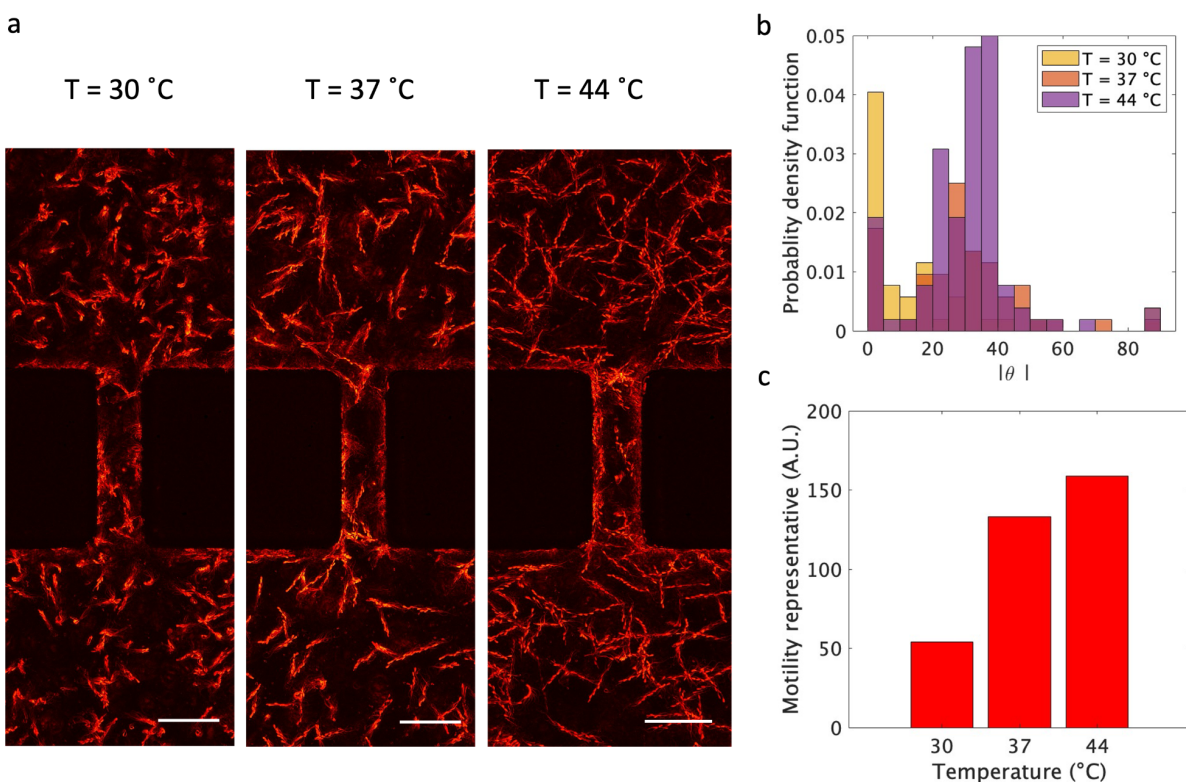
Figure S5. Effect of temperature on scattering angle and motility of sperm. (a) comparing sperm distribution at different temperatures (30, 37, and 44 °C) under no flow condition. Images are obtained by overlaying 10 consecutive frames and colorizing gray-scale images. Red pixels show the sperm presence in the observation window. Scale bar indicates 100 μm. (b) compares the probability density function of scattering angles measured during 9 seconds of videos. (c) motility representative of sperm population on upper zone of barrier calculated from the overlayed image of 5-second video for different temperatures.

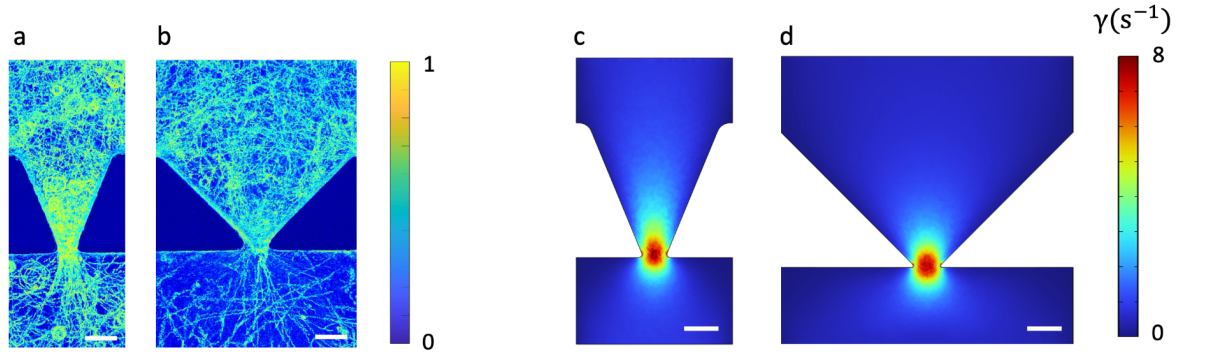## S5. Effect of tapered barriers on sperm navigational pattern

Figure S6. Comparing sperm navigation and shear rate profile in barriers with different taperness. Navigational pattern of sperm population in barriers with taperness of 45° (a) and 90° (b). Color bar indicates the intensity of pixels. Scale bar is 100 µm. (c) and (d) are shear rate profiles of 45 and 90° barriers under same portal shear rate ($\gamma = 8\ s^{-1}$) extracted from simulation using COMSOL software. Scale bar indicates 100 µm. Color bar shows the local shear rate.

S6. Effect of barrier port size on sperm navigation

To simulate the pathways created due to folded-ness of the fallopian tube or local muscular contractions, the port size of a 45°-tapered barrier increased from 85 µm to 130 and 230 µm and the navigation of sperm population was studied. Figure S7. a to c compares the navigational patterns resulting from overlaying a 5-second video for 85, 130, and 230 µm port size barriers, respectively. The inlet flow condition to all chips was kept the same, therefore, increasing the port size resulted in a decrease in port shear rate from 8 to 5 and 3 s^{-1} for port sizes of 130 and 230 µm. Decreasing the port shear rate decreases the motility-based selection of barriers and more sperm can pass it, therefore higher directionality is expected. Figure S7.d compares the directionality for different port sizes. As expected, increasing the gap size increases the directionality due to smoothing the shear rate constraint in the port, and hence, more sperm with lower velocities can also pass(*4*). directionality peaks at the port size corresponding to lowest shear rate required for rheotactic motion at around 116%. In this case, barriers have highest directionality and lowest selectivity. The median directionality of three port sizes (w_1) were fitted to a logistic function ($R^2 = 1$)

$$directionality\ (\%) = \frac{a}{1 + exp\ exp\ (-b(w_1 - c\ ))}$$

where a, b, and c are 117, 0.04, and 96 respectively.

To further assess the directionality in very large port sizes, we made a no-barrier chip by manually removing barriers from the chip. We assigned this barrier type to the condition when port size is double of the critical value (required for rheotactic reorientation). At this port size, the shear rate is 1.5 s^{-1} and no rheotaxis should not be observed. As expected, directionality of extremely large port sizes is 100 %, meaning that there is no active navigation of sperm and only

the rotational diffusion dominates the system, and a few sperm remain on the surface of the channel. In terms of accumulation index, increasing the port size reduced the accumulation of sperm in the barrier due to reduced area with appropriate rheotaxis shear rate.
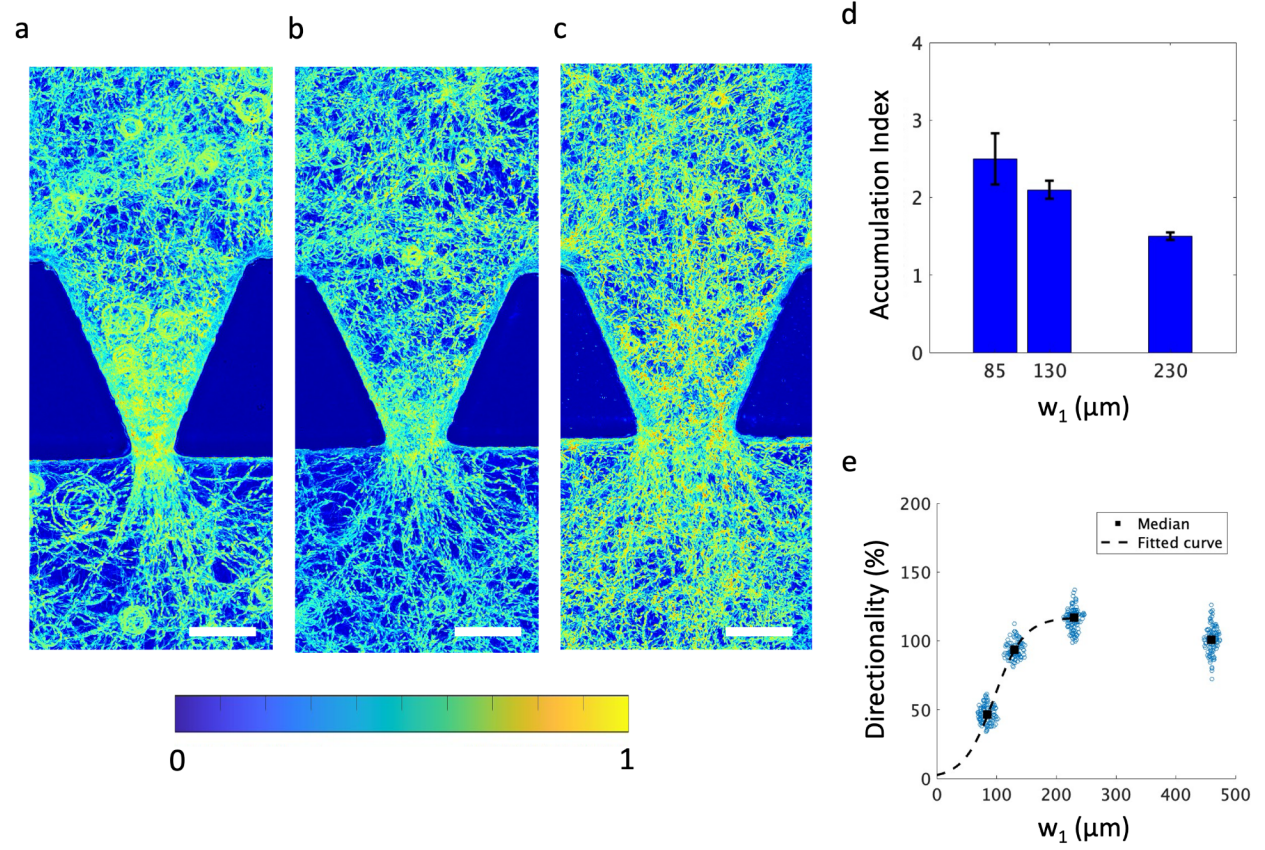

Figure S7. Effect of barrier port size on sperm navigation and accumulation in 45° -tapered barrier under same inlet flow conditions. Color bars indicate intensity of pixels. Scale bar shows 100 μm. (d) directionality versus port size of barrier. Corresponding portal shear rates are 8, 5, and 3 s^{-1} respectably. Dashed line indicates the fitted curve to the main data point. (e) average accumulation index versus port size. Error bars indicate standard deviation. Accumulation index is calculated for three identical barriers of each type.

Supporting Movies

Movie S1. Time lapse of transient navigatonality change by adding fluid flow to straight barrier

Movie S2. Effect of portal shear rate on sperm navigation in straight barrier

Movie S3. Motility and sperm distribution in the vicinity of a straight barrier at different temperatures

Movie S4. Sperm navigation in barriers with two different tapered angles

Movie S5. Sperm navigation in tapered barriers with increased port size

Movie S6. Hydrodynamic sperm cooperation in tapered barrier

References

1. M. Yaghoobi, A. Abdelhady, A. Favakeh, P. Xie, S. Cheung, A. Mokhtare, Y. L. Lee, A. V. Nguyen, G. Palermo, Z. Rosenwaks, S. H. Cheong, A. Abbaspourrad, Faster sperm selected by rheotaxis leads to superior early embryonic development in vitro. *Lab. Chip* **24**, 210–223 (2024).

2. S. Boryshpolets, S. Perez-Cerezales, M. Eisenbach, Behavioral mechanism of human sperm in thermotaxis: A role for hyperactivation. *Hum. Reprod. Oxf. Engl.* **30** (2015).

3. I. P. Oyeyipo, M. van der Linde, S. S. du Plessis, Environmental Exposure of Sperm Sex-Chromosomes: A Gender Selection Technique. *Toxicol. Res.* **33**, 315–323 (2017).

4. M. Zaferani, G. D. Palermo, A. Abbaspourrad, Strictures of a microchannel impose fierce competition to select for highly motile sperm. *Sci. Adv.* **5**, eaav2111 (2019).